ForceSight: Non-Contact Force Sensing with Laser Speckle Imaging

Siyou Pei
University of California, Los Angeles
Los Angeles, CA, USA
sypei@ucla.edu

Pradyumna Chari
University of California, Los Angeles
Los Angeles, CA, USA
pradyumnac@ucla.edu

Xue Wang
University of California, Los Angeles
Los Angeles, CA, USA
xw526@ucla.edu

Xiaoying Yang
University of California, Los Angeles
Los Angeles, CA, USA
xiaoyingy@ucla.edu

Achuta Kadambi
University of California, Los Angeles
Los Angeles, CA, USA
achuta@ee.ucla.edu

Yang Zhang
University of California, Los Angeles
Los Angeles, CA, USA
yangzhang@ucla.edu

ABSTRACT

Force sensing has been a key enabling technology for a wide range of interfaces such as digitally enhanced body and world surfaces for touch interactions. Additionally, force often contains rich contextual information about user activities and can be used to enhance machine perception for improved user and environment awareness. To sense force, conventional approaches rely on contact sensors made of pressure-sensitive materials such as piezo films/discs or force-sensitive resistors. We present *ForceSight*, a non-contact force sensing approach using laser speckle imaging. Our key observation is that object surfaces deform in the presence of force. This deformation, though very minute, manifests as observable and discernible laser speckle shifts, which we leverage to sense the applied force. This non-contact force-sensing capability opens up new opportunities for rich interactions and can be used to power user-/environment-aware interfaces. We first built and verified the model of laser speckle shift with surface deformations. To investigate the feasibility of our approach, we conducted studies on metal, plastic, wood, along with a wide variety of materials. Additionally, we included supplementary tests to fully tease out the performance of our approach. Finally, we demonstrated the applicability of *ForceSight* with several demonstrative example applications.

CCS CONCEPTS

• **Hardware** → **Sensors and actuators**; **Sensor applications and deployments**; • **Human-centered computing** → **Human computer interaction (HCI)**.

KEYWORDS

Force sensing, Non-contact sensing, Laser speckle imaging, Ubiquitous computing

1 INTRODUCTION

Force is a ubiquitous signal that occurs when objects are in contact. As a side product of human activities in environments, force reveals unique information and force sensing has a wide range of use cases in ubiquitous computing and human-computer interaction. For instance, touch interactions such as discrete button touches, swipes, and scrolling induce force between user fingers and interaction mediums such as buttons, glass panels, and skin. Robots rely on force as critical feedback for object manipulation. Moreover, the sensed force can be used to derive a rich set of second-order signals. For example, force applied to host surfaces by objects reveals their weights. Sensing the force between user fingers and contact surfaces adds an additional dimension to touch interactions. All these signals constitute rich information that intelligent vision-based sensing systems could leverage in addition to RGB and depth to become more robust, accurate, and even privacy-preserving.

In this paper, we consider only normal force, applied to objects in contact perpendicular to the contacting surfaces. To sense this force, conventional approaches instrument sensors (e.g., Force Sensitive Resistor) on surfaces, or in between objects. This contact-based sensing approach either requires wiring which can be inflexible to deploy, or runs on battery-powered wireless sensor systems, which is costly to scale and maintain. Additionally, contact-based sensors could be sensitive to exposure of elements, and thus can be prone to error without periodical calibrations. These inborn challenges of the contact-based approach eliminate sensing opportunities for a wide range of low-cost and passive objects such as 3D prints and room utilities (e.g., walls, tables, faucets). There are also scenarios where contact-based sensors might not be preferable such as on-body interactions, from a user experience perspective.

To address these challenges, we create a non-contact force sensing approach based on laser speckle imaging, a well-known imaging technique commonly used for medical applications (e.g., blood flow assessment) but now adapted to enable non-contact sensing for ubiquitous force signals that a wide array of interactive systems could leverage. Specifically, we detect minute deformations of surfaces when force is present. Our key observation is that laser

speckles change significantly at surface deformations, even with very small magnitude. Because laser speckles are caused by scattered signals added constructively and destructively depending on their relative phases, surface deformations of the same order of magnitude as the laser wavelength (several hundred nanometers) can alter laser speckles significantly. During the course of surface deformations, the changes of laser speckles have structured spatial and temporal patterns that correlate with the amount of force applied. Our system, which mainly consists of a defocused camera, a laser source, and signal-processing algorithms, detects these structured patterns to infer the amount of force.

In this research, we first conducted a series of benchmark tests with common everyday materials and a high-precision force-sensing linear actuator to verify our sensing principle. Then we established a calibration process for later evaluation. Our core signal-processing algorithm features optic flow displacement tracking and denoised aggregation. We investigated two sensing configurations – one is the *diverged laser setting*, with a diverged laser beam covering a wide surface area in which force could happen anywhere inside; the other is the *focused laser setting*, which uses a focused laser beam to sense force at known locations. Finally, we conducted an evaluation that systematically investigated *ForceSight* with three common materials – wood, plastic, and metal of various sizes and thicknesses, and at various distances with two calibration methods. We also investigated a wide spectrum of factors in supplemental studies to fully tease out the performance of our system. The results indicated a robust and accurate performance of our system, with all average errors across all materials and distances being less than 0.31 N. Finally, we demonstrate the applicability of our system with example applications. Overall, our contributions include:

- A theoretical model of laser speckle motion due to force-induced surface deformations.
- An end-to-end system including hardware and signal processing algorithms for non-contact force sensing based on laser speckle imaging.
- A systematic evaluation including two sensing configurations, two calibration procedures, and multiple series of tests to investigate the feasibility of the sensing approach.
- A representative set of example applications that demonstrate the expressivity of our proposed sensing approach.

2 RELATED WORK

2.1 Laser Sensing for Interactive Systems

Laser is widely used in sensing systems for being collimated and coherent – two unique properties that contribute to signal-to-noise ratio and high sensitivity respectively of laser-based sensing systems. Previous systems have leveraged collimated lasers (with low divergence) in creating interactive systems, e.g. Digits [14] uses angled line lasers to intersect fingers for finger position estimation and hand pose reconstruction. When modulated with RF frequencies as carrier waves, range-finding laser beams (i.e. LiDAR). have long been used to build interactive surfaces (e.g., The LaserWall [21, 22] and SurfaceSight [16]). A different object tracking principle using feedback loops featuring a movable mirror platform and a camera has been shown [3]. Lumitrack [40] used films in concert with lasers to have structured light patterns on ambient optical

sensors for 3D tracking. Due to the high coherence, constructive and destructive interferences between reflected laser wavefront result in light patterns of bright and dark dots respectively. This light pattern is called laser speckle, which has been thoroughly explained by Zizka et al. [46]. Next, we review prior work using this phenomenon, which *ForceSight* also leverages.

2.2 Laser Speckle Imaging

First, it is possible to have laser travel inside the transmission medium, which alters the laser path resulting in distinctive interference that encodes information into laser speckle patterns. For example, Li et al. [17] used laser speckles to detect perturbations of optic fibers. Kim et al. [15] used a similar principle to detect deformations of a scotch tape, through which pressure inside the cavity can be detected remotely. Note that it is possible to use non-laser optical approaches to detect surface deformations (e.g., [4, 8]), the use of laser by its nature of active sensing significantly improves the SNR and thus lowers the complexity of hardware and software.

Closer to our setup is prior work that detected laser speckles induced by the reflections of object surfaces. Prior work has demonstrated laser as carrier signals to reveal material type information [6, 25]. Jo et al. [13] and Smith et al. [32] leveraged the sensitivity of laser speckle to surface displacements to track objects in 3D space. With high-speed cameras, spatial correlations between speckle patterns in frames when objects are in motion can be preserved. Even fingertips can be tracked for micro-gesture input [31]. This sensing principle is akin to how a laser-based optical mouse tracks its position on 2D surfaces. SpeckleSense [46] and SpeckleEye [20] demonstrated low-cost and high-speed sensors in multiple configurations that enable rich interactive applications. It is also possible to detect second-order signals derived from this laser speckle shift caused by surface displacements. Shih et al. [30] demonstrated laser speckle imaging in surface tampering detection. Surface waves caused by in-air acoustic signals or vibrations from built-in motors can also be detected remotely with laser speckle shifts [28, 38, 44, 45].

Closest to our work are Laser Speckle Imaging systems in the medical domain, with their capability to sense surface deformations over time at microscales. Researchers have used defused laser on body tissues to image blood flow. The slight deformations of microvasculature due to blood flow cause minute laser speckles movements. These movements generate blurred local regions on images [2, 7]. This sensing principle is easy to set up, low-cost to implement, and has shown a wide array of use cases in clinical settings (e.g., Dermatology [11], Ophthalmology [35], and Neurology [23]). For a complete review of laser speckle's clinical applications, we recommend Heeman et al. [9].

3 MODELING LASER SPECKLE

3.1 Laser Speckle Pattern on Rough Surfaces

When rough surfaces are illuminated by laser beams, a random interference pattern will be observed on the image plane, called laser speckle [1]. To elaborate, a whole diffuse surface can be regarded as being composed of massive independent scattering surface elements, which result in statistically independent phases of the
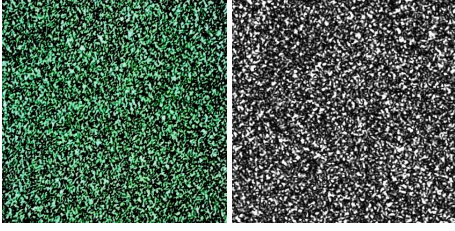
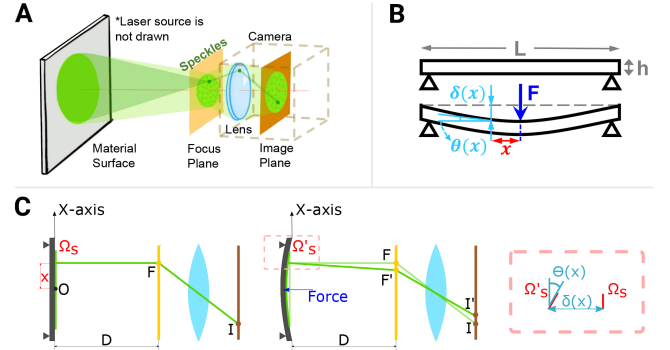Figure 1: Left: Real speckles. Right: Simulated speckles.

Figure 2: *ForceSight* Modeling. A: Configuration of laser speckle imaging. A defocused camera captures speckles formed by laser beams reflected from the material surface. B: Deformation model. C: Due to surface deformation at force, a laser beam reflected by the micro-surface Ω_s changes its imaging position from I to I' on the image plane. Left: no force applied. Center: force applied at O. Right: zoomed-in micro-surface.

reflected laser beams. These non-coherent beams add up constructively and destructively as they traverse in space, forming granular patterns of random distribution on the image plane.

To efficiently verify laser speckle forming, we built the model in simulation. We use a Gaussian beam to simulate an incident laser over a uniform random rough surface $\Phi(x, y)$. Beam distribution $g(x, y)$ on the rough surface can be described as Eq. 1 [36].

$$g(x, y) = \frac{\omega_0}{\omega} e^{\left[-(x^2+y^2)(\frac{1}{\omega^2}+\frac{ik}{2\rho}) - ikd \right]} \qquad (1)$$

where ω_0 and ω are the waist radius, and illuminated beam spot radius, respectively. (x, y) refers to the location on the rough surface. $k = \frac{2\pi}{\lambda}$ in which λ is the wavelength of Gaussian beam. ρ means the wave-front curvature radius. d is the shortest distance between the laser source and the rough surface. The back-scattered light can be modeled by the Fresnel diffraction [29].

To validate our simulation, we collected real-world laser speckles on a white wall using a USB camera with a resolution of 2592×1944. The laser speckles were induced by a 10 mW 532 nm green laser (12-degree divergence), positioned 10 cm away from the wall. The real-world speckles and simulated speckles are shown in Fig. 1. The simulated speckles resemble real speckles in terms of their size and shape, though the overall distribution is sparser for the difference between the wall surface and the random rough surface.

With the subtle deformation of the object surface, speckle patterns of adjacent timeframes have high similarity, which allows speckle motion tracking. However, the speckle patterns can also "boi", meaning the speckles can tumble randomly fading in and out and the original spatial structure of patterns alters. In general, speckle motion appears as a combination of speckle translation and boiling, since the speckle deformation would occur inevitably [34]. To compensate for the boiling effect, as we will show later in the paper, we designed our algorithm so that spatial continuity is not a prerequisite, i.e., we do not track the same set of speckles over long distances on the image plane.

3.2 Laser Speckle Motion Due to Surface Deformation

In this section, we derive a theoretical *speckle flow* model to explain how the laser speckle patterns change due to surface deformations in the presence of force.

3.2.1 Deformation Model. For simplicity of exposition without loss of generality, we frame the physical model as applying a concentrated load to the center of a rectangular plate with edges simply supported. Assuming the plate is isotropic and homogeneous, we

can simplify the problem by looking at its transverse cross-section. As shown in Fig. 2 B, f is the point load actuated at the center of the beam, and x is the distance from the center to a point of interest. $\delta(x, f)$ and $\theta(x, f)$ are the plate deformation distance (i.e., deflection) and the angle in radians at the point of interest, respectively. δ_{max} is the maximum deflection which locates at the plate center. The θ is defined as 0 when the plate is not deformed. The equations of the deflection and angle are as follows [19, p. 330–331],

$$\delta(x, f) = \frac{f}{48EI_s}(L^3 - 6Lx^2 + 4x^3) \qquad 0 \le x \le L/2 \quad (2)$$

$$\delta(x, f)|_{x=0} = \delta_{max}(f) = \frac{fL^3}{48EI_s} \qquad (3)$$

$$\theta(x, f) = \frac{f}{4EI_s}(Lx - x^2) \qquad 0 \le x \le L/2 \quad (4)$$

$$\theta(x, f)|_{x=\frac{L}{2}} = \theta_{max} = \frac{fL^2}{16EI_s} \qquad (5)$$

where E is the Young's Modulus, I_s is the moment of inertia of the material plate, and L is the side length of the plate. The formulas indicate that the deflection, scales linearly with the magnitude of applied force, as verified in Section 3.3 (Fig. 3 Right).

3.2.2 Micro-Surface Hypothesis. We use the following hypothesis to approximate our surface for the sensing principle. A surface can be divided into multiple small sub-surfaces, as Fig. 2 C shows. When a sub-surface is small enough, its area becomes insignificant for our interest. We define such a sub-surface, as a *micro-surface*. If we look from the side, the surface plate is idealized as a polygonal line combining line segments of all micro-surfaces.

3.2.3 Speckle Motion due to Surface Deformation. As shown in Fig. 2 C, in 2D space, the location, deflection, and angle of a micro-surface are respectively represented by x (distance from plate center to the micro-surface), δ, and θ. Proof in 3D space is a symmetry-based extension of our discussion in 2D space, with 3D coordinates

and normal vectors. Given that the deformation model is isotropic on the homogeneous plate, we will move on to prove it in 2D space which is more concise and clear.

Statement: The speckle motion goes towards the contact point in the presence of force. The motion displacement on the image plate can be described by

$$\Delta I = aD\frac{f_0}{4EI_s}(Lx - x^2) \qquad 0 \le x \le L/2 \qquad (6)$$

where a is a scaling factor of focus-image projection model, D is the focus-surface distance, f_0 is actual force, L is the length, x is the $\Omega_s - O$ distance (from the micro-surface to the plate center).

Configuration: As shown in Fig. 2 A and C, our model consists of a laser, a material surface (i.e., the plate in the previous discussion), and a camera with a focus lens, a focus plane, and an image plane. The focus plane denotes the plane where objects are in focus, whose position can be deduced from the Thin Lens Equation. The camera is defocused, thus speckle motion is obvious while the imaging of surface is blurry, preserving the SNR of our setup by not letting surface textures register on the image plane. The coordinate system origin is O, which is set to the intersection of the material surface and optical axis of the lens. The surface center is also configured at O. The original surface is D m away from the focus plane.

Proof: Suppose we have a micro-surface Ω_s which is x away from the origin O. A laser beam is reflected by Ω_s onto the focus plane at F. We call F a focus point (a point in focus, not a "focal point"). With no force, its deflection $\delta(x, f)|_{f=0} = 0$ and deformation angle $\theta(x, f)|_{f=0} = 0$. F registers a conjugate point I on the image plane.

Now, a small force is applied at the surface center. It pushes the micro-surface Ω_s all the way to Ω_s' with deflection δ and deformation angle θ. As a result, the focus point F shifts to F', and the conjugate point I moves to I' accordingly, toward the touch center. The deflection, angle, and speckle motion can be modeled as below,

$$\delta(x, f)|_{f=f_0} = \frac{f_0}{48EI_s}(L^3 - 6Lx^2 + 4x^3) \qquad (7)$$

$$\theta(x, f)|_{f=f_0} = \frac{f_0}{4EI_s}(Lx - x^2) \qquad (8)$$

$$\Delta I = a\Delta F = a|F' - F| = a(D + \delta(x, f_0))\tan\theta(x, f_0) \qquad (9)$$

Given our configuration where the D (m) is much larger than the surface deformation (from nm to mm), the model can be approximated as

$$\Delta I \approx aD\tan\theta(x, f) = aD\frac{f_0}{4EI_s}(Lx - x^2) \qquad (10)$$

From this speckle motion model, we can draw several observations, which we also drew from validation in Section 3.3:

(1) The speckle motion ΔI is linearly correlated with force f.
(2) The speckle motion ΔI grows as the distance D increases.
(3) Given $I_s = \frac{wh^3}{12}$, where w and h are the width and thickness of the material surface plate, the speckle motion δI is proportional to the inverse of the cube of thickness h.
(4) When the stiffness increases (i.e., the Young's Modulus E is larger), the speckle motion ΔI decreases.

3.3 Sensing Principle Validation

We collected data to verify our sensing principle and modeling. A motor-based linear actuator was used (see Fig. 5 Right) to actuate a
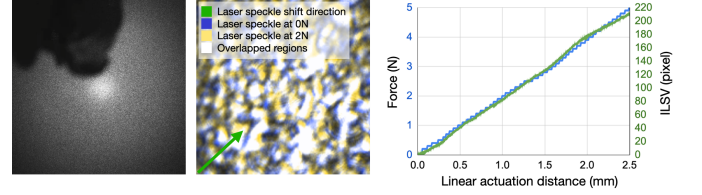

Figure 3: Sensing principle validated with a linear actuator setup. Left: raw laser speckle. Center: highlighted speckle shift due to the surface deformation caused by an applied force of 2 N. Right: Integrated Laser Speckle Velocity correlates with the applied force.
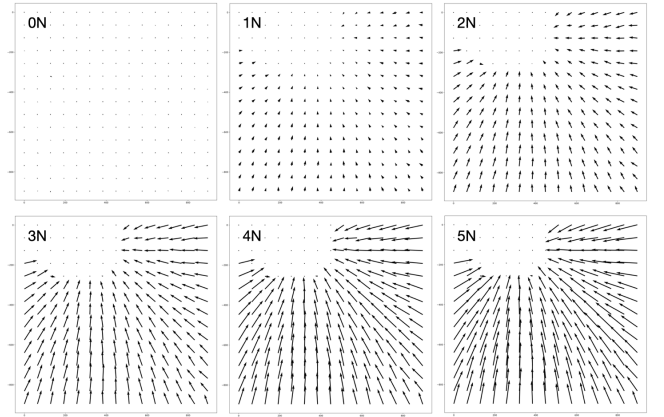

Figure 4: Fields of Integrated Laser Speckle Velocity in presence of different amounts of force, forming a centripetal pattern towards the force centers.

60.96 cm square metal surface which measured 1.59 mm ($\frac{1}{16}$") thick. Surface deformation was measured by counting motor steps (at 0.78 μm resolution) while the applied force was measured with the force meter affixed to the linear actuator's indenter. We bundled a camera with a diverged laser as shown in Fig. 5 Left (Details of this sensor bundle can be found in Section 4.1) and placed them above the surface. The linear actuator pushed the surface until the force reached 5 N. Data was streamed to a PC through USB.

Fig. 3 Left shows the raw laser speckles, while Fig. 3 Center highlights distinctive laser shifts (observed at 10 cm from the point of the applied force of 0 N vs. 2 N). The laser was focused during the data collection for better visualization of the laser speckle shifts, avoiding quantization in images (due to relatively small speckle sizes induced by diverged lasers). These shifts were due to small surface deformations caused by the applied force. We use optical flow to calculate the distance of laser speckle shift between adjacent frames, called *laser speckle velocity* (LSV). Note that LSV was referred to as the speckle motion in our modeling section. Fig. 3 Right plots the integral of LSV (ILSV) and the applied force over linear actuation distance across the entire image frame excluding regions occluded by the sensor bundle. The ILSV correlates with the amount of force. We also plot out the ILSV across a larger region (900×900 pixels) in the presence of 0 N, 1 N, 2 N, 3 N, 4 N, and 5 N
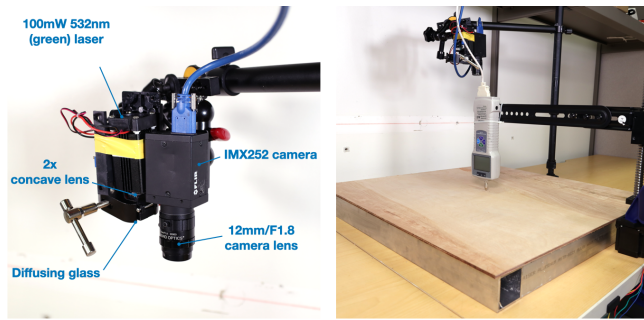
Figure 5: Left: *ForceSight* **sensor bundle. Right: evaluation setup with the force gauge mounted on a linear actuator.**

forces respectively, as shown in Fig. 4. The length and direction of each quiver indicate the normalized magnitude and the direction of ILSV. It shows a centripetal pattern towards the force centers, with growing magnitudes as the force increases.

Overall, these results verify the sensing principle that the rest of our paper builds upon. Therefore, we can average ILSV magnitudes to get a robust indicator signal of *ForceSight* for force estimation. For higher accuracy, our force-sensing algorithm uses the magnitude projected onto the direction toward the force center for a weighted aggregation, which will be further described in Section 4.2.2.

3.4 Calibration Exploration

The test surfaces are simplifications of real-world objects which are often complex (e.g., uneven surfaces, irregular shapes, varying thicknesses, and heterogeneous material compositions). Modeling this level of complexity requires precise sensory systems (e.g., 3D scanners) and intense calculations. In comparison, *calibration* is a more viable path for its simple setup process so long as the signal has high repeatability or the algorithm can cope with shifts in signals over time and configuration changes. In fact, calibration is a common technique in Laser Speckle Imaging – for example, Laser Speckle Contrast Imaging requires captured data as a baseline [30]. Calibration is also common in force-sensing applications. For example, once FSR is inserted, it needs calibration to map its resistance to the amount of force. Therefore, we set out to design *ForceSight* with this empirical approach, to develop algorithms with minimal calibration needed in practical force-sensing applications.

4 IMPLEMENTATION

4.1 Sensor Bundle

Our sensor (Fig. 5 Left) consists of a camera (FLIR GS3-U3-32S4M-C 1/1.8" Grasshopper®3 1536×2048) and a 532 nm (green) 100 mW point laser projector (from Civil Laser). We use the camera at its highest frame rate 121 fps with a fixed 4 mm/F1.8 lens (Edmund Optics) throughout the evaluation, with the camera out-of-focus such that its working distance from front housing is adjusted to 0 mm. A 532 nm camera filter is attached to the camera for better SNR. The camera and the laser projector are bundled, pointing in the same direction. The camera can capture speckles from the diffuse reflection of the laser on an object's surface.

We explore two configurations for the laser in our sensor bundle, the diverged mode, and the focused mode. In diverged mode, the laser is diverged and expanded with three concave lenses (two LD2568-A with -9.0 mm focal length and one LD2060-A with -15.0 mm focal length from Thorlabs) and one optical diffuser (HOLO 80 Deg 12.5mm from Edmund Optics), so the green laser can spread over a whole surface. In focused mode, the laser beam remains as a dot when it is landed on the object's surface, concentrating energy for long-distance sensing applications.

4.2 Algorithm

The output of our sensor setup is an ordered stack of video frames $\left\{\mathbf{v}^k\right\}_{k=0}^{N-1}$, where N is the total number of frames. We assume that the video is captured at a frame rate f. Our goals from this framestack are twofold: first, we want to reliably estimate speckle velocity fields; and second, to estimate the applied force in real-time. These aspects are discussed below sequentially.

4.2.1 Speckle Velocity Fields. The speckle frames have distinctive structures. Qualitatively, as a result of applied force, the speckle patterns show distinctive centripetal displacement. On smaller time scales, these can be approximated as local pattern translations. However, across larger timeframes, scale differences may also be observed in local patterns. Given these observations, we set up the velocity field estimation problem as a flow estimation problem across small timeframes. That is, we estimate flow displacement across every two adjacent timeframes, thereby obtaining a correlated metric to the flow velocity. The flow displacement is used as a proportional estimate for laser speckle velocity. Algorithm 1 includes pseudocode for this simple algorithm.

Algorithm 1 Speckle velocity field estimation

Input:

Frame stack $\left\{\mathbf{v}^k\right\}_{k=0}^{N-1}$, number of frames N, video frame rate f, Optical flow operator OpticalFlow $\{\cdot, \cdot\}$

Output:

speckle velocity stack $\left\{\mathbf{r}^k\right\}_{k=0}^{N-2}$

1: Initialize $\left\{\mathbf{r}^k \leftarrow 0 \ \forall \ k \in \{0, 1 \ldots N - 2\}\right\}$
2: **for** $i = [0, N - 2]$ **do**
3:     $\mathbf{r}^i \leftarrow$ OpticalFlow $\left\{\mathbf{v}^i, \mathbf{v}^{i+1}\right\}$
4: **end for**
5: **return** $\left\{\mathbf{r}^k\right\}_{k=0}^{N-2}$

4.2.2 Real-time Force Estimation. Qualitatively, the applied force on the surface and temporal integral of the speckle velocity are directly correlated. Therefore, given the material and its physical configuration, a mapping may be learned to infer applied force from the integral of the estimated speckle velocity. The estimate speckle velocity is calculated by averaging projected lengths of all vectors within the image frame, towards the estimated force center. Note that this gives us a signed measure for the estimated speckle velocity. A cumulative sum of (i.e., integral) the estimated speckle velocity over time is then directly used by regression models to estimate the instantaneous applied force.
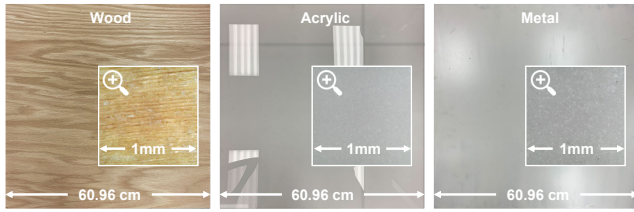
Figure 6: Photos and microscopic images of materials. The actual side lengths of global photos and zoom-in images are 60.96 cm and 1 mm respectively.

5 EVALUATION

5.1 Apparatus

As shown in Fig. 5 Right, a force curve gauge (resolution 0.1 N) is mounted on a linear actuator (resolution $7.8125x10^{-7}$ m/step), pointing towards the object surface. The sensor bundle was placed above the surface. The surface was supported on its edges by an aluminum frame base. The ground truth force reading from the force curve gauge and the raw data from the camera were streamed to a computer. The linear actuator was also connected to the computer for control.

5.2 Test Materials

Our test apparatus involved sheets of three types of materials (wood, acrylic, and metal) which are common to find in daily settings. These square sheets measured 60.96 cm long and of a variety of thicknesses, which are common building materials purchased from home improvement retailers [5, 24, 33]. To measure the roughness of these materials, we conducted a friction test using a 3D printed PLA instrument with a force gauge to measure the coefficients of friction. For the three type of materials we tested, their coefficients of friction measured 0.334, 0.417, and 0.301 for wood, acrylic, and metal. Fig. 6 shows a closer view of them.

- wood: 5 mm, 5.56 mm (7/32"), 6.35 mm (1/4")
- acrylic: 1.59 mm (1/16"), 3.18 mm (1/8"), 6.35 mm (1/4")
- metal: 0.79 mm (1/32"), 1.59 mm (1/16"), 3.18 mm (1/8")

5.3 Data Collection Procedures

We describe the procedures for one complete trial of data collection in this section. The first step was pre-collection preparation. Placed on top of the aluminum frame base, the sheet was simply supported by its four edges. The sensor bundle was then adjusted carefully for the correct working distance and laser coverage (i.e., diverged vs. focused modes). We also adjusted the camera's exposure time and gain in software to ensure a clear view of laser speckles. Besides, we set the indenter of the force curve gauge to hover above the centroid of the sheet. The reading of the force curve gauge was 0.0 N at the beginning of each data collection trial.

We started data collection once the setup was ready. As the linear actuator went downwards at a speed of 6.7208×10^{-2} mm/s, the indenter of the force curve gauge approached the sheet surface with a force reading of 0.0 N. Once the indenter got in contact with the surface, the force reading started to increase as the actuated force incremented. Once the force reached 5.0 N, the force curve gauge started to retract until the reading returned to 0.0 N. The speckle images (with a resolution of 1536×2048 at 121 fps), force readings (with a resolution of 0.1 N at 10 fps), and indenter displacement (counted in steps) were saved during this push-release process with synchronized timestamps. After the process, we recorded the location of the indenter (x_c, y_c).

The next step was post-processing. We applied a mask to remove regions where speckles were induced on the linear actuator as opposed to the tested sheet. In real-world applications, this mask could be easily generated using depth cameras. We also set a threshold to get rid of regions that were too dark.

Following the procedure above, the collected data is called one "trial" for the given object sheet. Each trial took from 40 to 85 seconds to complete, depending on the elasticity of the material of the tested sheet. Five trials were collected per sheet. In total, we collected 2625 seconds of data with 317625 images, 2625 force readings, and 225830 linear actuator steps.

5.4 Train-Test/Calibration Procedures

We evaluated *ForceSight* in two procedures, each following a unique calibration process that could be used in real-world scenarios. Note that we use "train" and "test" to explain the data split in building and evaluating our regression models, though we did not use machine learning in *ForceSight*.

Procedure#1: Train-Test split by trials. In this procedure, we split the five trials into train trials and test trials with different split percentages. For example, the train-test split percentage is $1/(1 + 4) = 20\%$ when we build the regression model on one trial and test it on the other four trials. Different combinations under the same percentages are grouped in an N-fold manner. This is to reflect a common real-world calibration process where sensors are calibrated with a full dynamic range of future signals to expect.

Procedure#2: Train-Test split by force. In this procedure, we first bucketed one trial of data (0-5 N) into five equal 1 N-range bins, and split the bins into train bin(s) and test bin(s) with different split percentages. For instance, the split percentage 40% indicates the regression model is built on forces in the first two bins and tested on the three remaining bins. Additionally, the train portion always starts from 0 N, and the test portion always follows the end of the train portion. It reflects another real-world scenario where sensors are calibrated with partial dynamic ranges of the future signals to expect. This is inherently challenging but could yield useful insights into the generalizability of the model.

In both procedures, we varied the amount of data in building the regression model, from 20 % to 80 % (i.e., 1-4 trials in Procedure#1, and 1-4 Newton range in Procedure#2). We evaluated our regression models with all train-test split combinations.

5.5 Results

We collected data in two settings, including one short sensing range with three materials (i.e., wood, acrylic, metal) using the diverged mode, and four long sensing ranges with one material (i.e., metal) using the focused mode. Additionally, we evaluated *ForceSight* with two train-test procedures. This evaluation process yielded four combinations, which we discuss in this section.
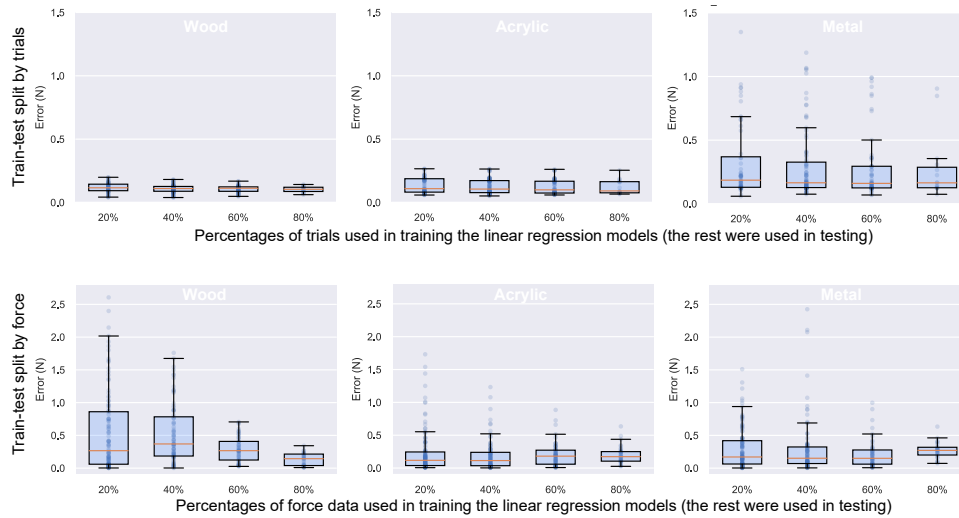
Figure 7: Evaluation results on sheets of three materials (wood, acrylic, metal) of various thicknesses.
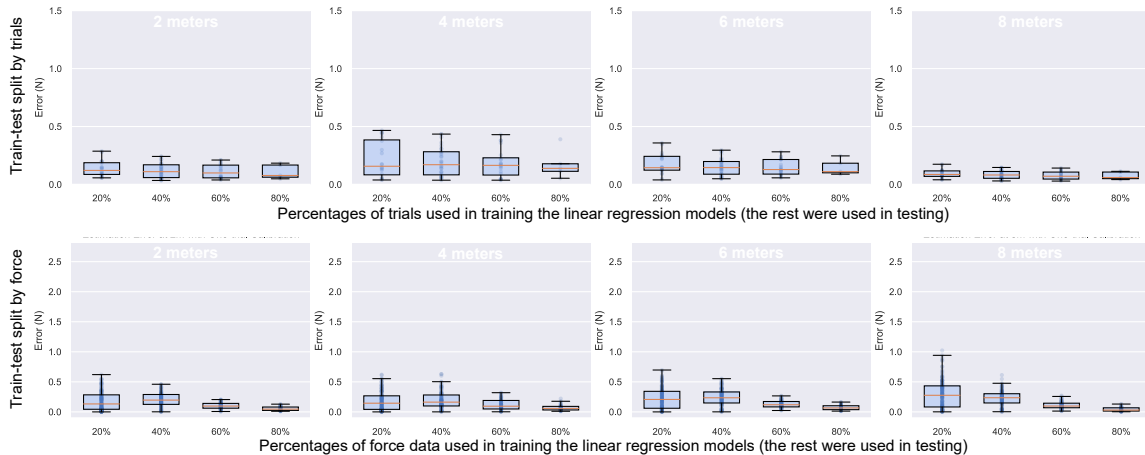

Figure 8: Evaluation results on four sensing distances (2 m, 4 m, 6 m, 8 m) tested on the metal sheet with a thickness of 1.59 mm (1/16").

5.5.1 Short Range Sensing (Diverged Mode). As Fig. 7 shows, *Force-Sight* achieves an averaged error of 0.18 N (SD=0.11) and 0.31 N (SD=0.12) for the two train-test procedures, respectively.

Train-Test split by trials. Comparatively, the train-test split by trials (i.e., calibrating the sensor with signals of full dynamic range) yielded better results. Among the three tested materials, *Wood* performs the best with the lowest averaged error of 0.11 N (SD=003) followed by *Acrylic* (error=0.13 N SD=0.06) and *Metal* (error=0.30 N SD=0.28). We found a significant source of error in the thickest metal sheet we tested (error=0.61 N, SD=0.31) for the small surface deformation resulting from the test force. Even with 5 N force, the surface deformation is almost invisible to naked eyes, though it can be detected by our sensor. We suspect that real-world applications with thick metal sheets would most likely involve stronger force, which could result in larger deformations and thus lower the errors

(or percentage errors). When comparing between percentages of the training data, we did not find any major differences. This result indicates that *ForceSight* can be calibrated very efficiently with a small amount of data.

Train-Test split by force. Train-Test split by force (i.e., calibrating the sensor with partial dynamic ranges) yielded an average error of 0.31 N (SD=0.12) across all materials. Interestingly, *Wood* performs the worst, with an average error of 0.44 N (SD=0.49) among all materials. Based on our observations, this was due to the heterogeneous internal microstructure distribution inside the wood sheets, resulting in non-linearity, which makes it harder for the regression model to generalize for unseen signals. When comparing between percentages of the training data, we did not find any major differences, pointing us again to the insight that *ForceSight* can be calibrated very efficiently with a small amount of data.

5.5.2 Long Range Sensing (Focused Mode). Fig. 8 shows that *Force-Sight* achieved an averaged 0.18 N (SD=0.05) and 0.18 N (SD=0.03) error for the two train-test procedures, respectively.

Train-Test split by trials. Again, the train-test split by trials yielded better results among the two procedures, which suggest calibration with signals of full sensing dynamic range for real-world applications. Among the four tested distances (2 m, 4 m, 6 m, 8 m), *ForceSight* yielded average errors of 0.12 N (SD=0.06), 0.20 N (SD=0.13), 0.16 N (SD=0.08), and 0.08 N (SD=0.04) respectively. We did not observe a clear correlation between distance and sensing performance, indicating the feasibility of *ForceSight* in long-range sensing. However, during the data collection, we observed more oscillations (i.e., noise) of laser speckles at longer sensing distances due to ambient vibration (e.g., airflow from HVAC, appliances running) and our algorithm is robust to these noises. We are cautious that severe vibrations from a longer sensing distance might require a superior denoise algorithm to process. Additionally, we did not find having more data in building regression models improves our sensing accuracy. This result is consistent with the outcome of the previous tests.

Train-Test split by force. Among the four tested distances (2 m, 4 m, 6 m, 8 m), results indicate average errors of 0.16 N (SD=0.13), 0.16 N (SD=0.14), 0.19 N (SD=0.15), and 0.21 N (SD=0.18) respectively. We did not find any linkage between distance and sensing performance. However, we found having more data in building the regression models improves our sensing accuracy.

5.6 Supplemental Studies

In supplemental studies, we investigated additional factors that could affect our sensing performance. Results from these additional factors further our understanding of this sensing technique and enrich its sensing vocabulary.

Angle of incidence. The angle of incidence has been a major factor in laser sensing performances due to the fact that reflected light energy increases as the laser gets perpendicular to the sensed surface. In this test, we collected data from various angles of incidence (from 0 to 40 degrees with a 10-degree internal), with a diverged laser positioned 30 cm away from the intersection point of its principal axis and the surface (i.e., 1.59 mm thick metal sheet), following the data collection and evaluation procedure as in our main evaluation. Results are shown in Fig. 9.

Overall, we noted an average error of 0.15 N (SD=0.06) and 0.13 N (SD=0.14) from calibration procedures #1 and #2 respectively. We did notice slight differences between performances when the sensor bundle is oriented with different angles of incidence, however, we did not see a trend that indicates a higher angle of incidence lowering the sensing performance. Though promising, we are cautious that more material types including ones that are more specular should be included in the test set.

Force location estimation. As a result of the centripetal displacement of the speckle patterns in response to force (e.g., a touch), the contact location is the common center for the estimated velocity vectors. We propose a center-estimation algorithm, which is essentially solving a distance-minimization problem. For a given center estimate, the error value is the sum of perpendicular distances of the point from all the estimated laser speckle velocity vectors for a
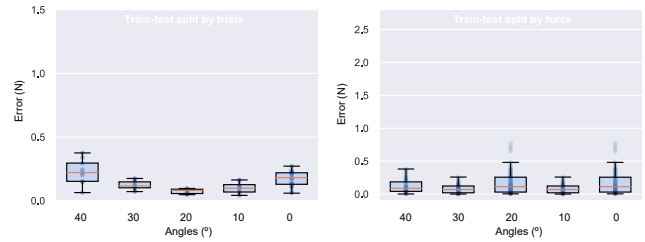

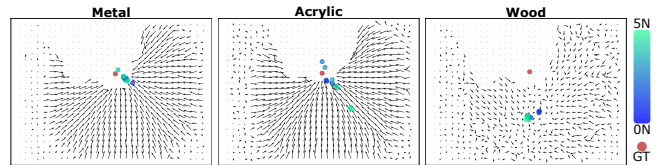**Figure 9: Evaluation results on the angle of incidence.**

Figure 10: Detecting force location on different materials using *ForceSight*. The ground truth force location is shown in red. Speckle velocity is shown in a log scale.

given velocity field. The point with a minimum error value is the best center estimate. We initialized a random center and then used gradient descent optimization. The algorithm is applied to a single frame with a learning rate of $\mu = 0.01$ and steps $T = 10,000$ in PyTorch. The final force location estimates are obtained by averaging over 10 random initialization and runs.

Figure 10 shows qualitative results on force location detection on the three materials (with the medium thicknesses). We note that we were able to approximately detect the force location for the metal and acrylic materials with mean Euclidean errors of 4.86 cm (STD of 1.66 cm) and 8.38 cm (STD of 6.00 cm) respectively. These results serve as proof of concept for *ForceSight* being a viable tool for not just force sensing but force location estimation as well. Notably, force location performs poorly on wood, as a result of its heterogeneous internal structure with a mean Euclidean error of 19.38 cm (STD of 1.09 cm). This establishes that the force location is limited in accuracy by the nature of material structures and resulting speckle motion features.

A wide array of materials. In this test, we included a wider set of materials and objects, including a book, pillow, package box, foam board, acrylic, wood, metal, and silicone. We collected one trial (0-5 N) of data for each material with a focused laser (i.e., focused mode) 30 cm away from surfaces and using the same procedure as previous tests. Force was applied 10 cm away from the laser dot on the tested surface. We built regression models that minimize errors (maximizing R^2) but included both linear and quadratic regression models in our search. Fig. 13 shows our results which indicate that simple models well fit data collected from these materials. We found *Book* to be the only object that requires a second-degree term among the test objects/material sheets. The distinctive coefficients across these materials can be used to identify material types. In this use case, *ForceSight* becomes a sensing instrument that yields elasticity of surfaces if the applied force is known.
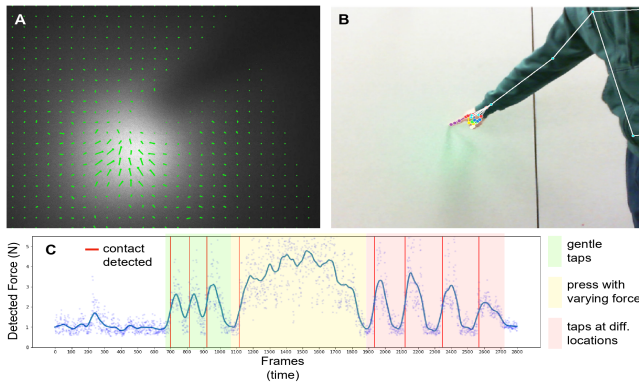
Figure 11: On-world true-force touch sensing. A: Integrated Laser Speckle Velocity Field overlaid on raw laser speckles. B: An RGB image captured by a webcam. C: Detected force from *ForceSight*. Of note that, to avoid optical flows induced by user motions, sensing is turned off at regions that are recognized as user body by MediaPipe pose tracking.
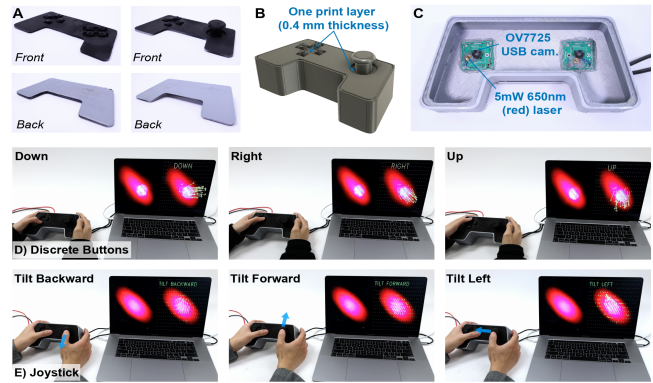

Figure 12: Interactive 3D prints using embedded *ForceSight* systems. A: Two designs of thin top plates that can transform user interactions into discernable plate deformations. B: 3D models of a controller. C: Two low-cost lite *ForceSight* bundles are embedded inside the controller. The rest of the figure shows live detection results of user interactions featuring discrete buttons and the joystick.

6 EXAMPLE APPLICATIONS

6.1 On-world Touch Sensing

Projected touch interfaces create ubiquitous interaction experience, which much prior work has investigated [39, 41, 42]. With depth cameras, touch sensing on everyday surfaces has never been easier. And yet, commodity depth cameras cannot sense fine-grained touch with small finger movements (sub-centimeter), as shown and discussed in prior work [41, 43]. However, being able to segment touch from minute motions without having users exaggerate their movements to accommodate for sensor inaccuracy is critical to fully utilize the expressive and natural interactions provided by touch. In this regard, *ForceSight* creates a potential solution using force as an additional signal to aid touch segmentation (touch vs. no touch). Fig. 11 shows the integrated laser speckle velocity field on office partitions when a user touches them at forces similar to ones on touchscreens. Note that we used Google MediaPipe [18] pose tracking to exclude regions of user bodies so that the detection pipeline is robust against interference from users' motion. *ForceSight* also works with a broader array of everyday surfaces including a fabric couch arm, a wood table, walls, and a fridge door.

6.2 3D Printing Interactivity

ForceSight also provides a viable path to 3D printing interactivity as many previous systems aim to achieve [26, 27, 37]. To achieve this, we embedded a lite version of *ForceSight* consisting of a 3 mW laser and a low-end webcam as in Fig. 12 C. The lite sensor bundle costs less than $20 to make. Fig. 12 D and E show example interactions enabled by the 3D printed controller with embedded *ForceSight*. *ForceSight* senses and recognizes the discernible surface deformations due to the applied force when users press the buttons and tilt the joystick in different directions. Since *ForceSight* sensor bundles are installed at the controller base, a user can easily switch controller top plates for applications that demand different interactions.

6.3 Force-based Material/Object Identification

Material identification has shown practical uses in HCI, as prior works demonstrated ID-enabled interactions [25] and material-aware laser cutting [6]. We notice that different materials exhibit distinguishable deformations in response to force due to variance in density and internal microstructures. For example, hard materials (e.g., wood) have a wider and shallow "footprint" whereas soft materials (e.g., silicone) deform locally around the force point resulting in a narrow and deep "footprint". The footprint geometry reveals much information about materials.

Another approach is to use regression model parameters as classifier features, which essentially convey Young's Modulus and the moment of inertia. Fig. 13 shows differences in parameters learned from our supplemental study *A Wide Array of Materials*, which can be leveraged for identification. We believe this force-based material identification can have broader applications in digital fabrications (e.g., water jetting) as well as object handling (i.e., robot arms can apply less amount of force when handling delicate materials).

6.4 Force-Aware Object Manipulation

Handling delicate objects requires force-sensitive mechanisms. Conventional methods rely on contact-based force sensors on robot
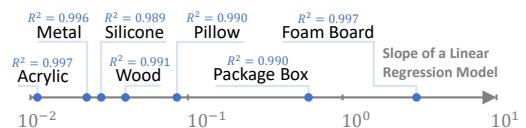

Figure 13: *ForceSight* builds a distinctive set of linear regression models for different materials/objects with high R^2. Coefficients of these models can in turn reveal the material type if the applied force is known, enabling material identification for richer applications.
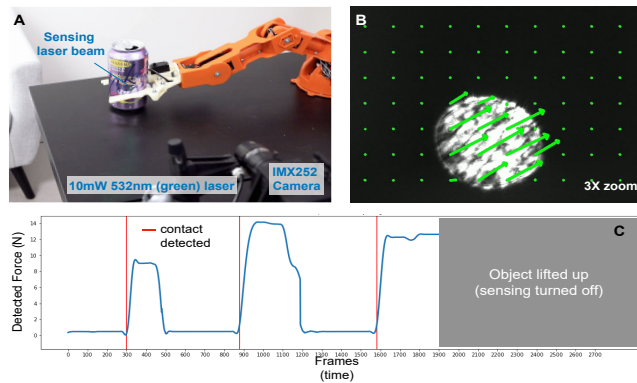
Figure 14: Remote force sensing for delicate object handling. A: Robotic arm grasps a soda can sequentially with three different forces – light, strong, and medium. B: Integrated Laser Speckle Velocity. C: Force detected by *ForceSight*.

arms. *ForceSight* creates a different approach to facilitate remote sensing which can potentially turn into centralized sensing in which one sensor can serve multiple robot arms under its field of view (akin to the sensing scheme of security cameras). Fig. 14 shows *ForceSight* working with a focused 10 mW laser and a low-cost robot arm (Arduino Braccio) to sense the grasping force on a soda can as a test primitive. ILSV is shown in Fig. 14 B. Once the force reaches the desirable amount, the robot arm starts lifting up the object (Fig. 14 C).

7 DISCUSSION

Laser safety The strongest laser used in *ForceSight* is 100 mW (Class III B) which is by itself hazardous for eye exposure. However, it is only used in diverged settings with wide divergence achieved by using three concave lenses concatenating with a diffusing glass. The divergence significantly shortens the Nominal Ocular Hazard Distance (NOHD) [10]. At our divergence (79.6 degrees), the NOHD is 5.09 cm. To further improve the safety of users, *ForceSight* could work with other sensing modalities such as RGB cameras and depth sensing – the laser can be turned off once users are too close. *ForceSight* could also use low-power guarding lasers [12] or deploy it at high installation/vantage locations, e.g., ceilings, to improve safety.

Laser power and color During experiments and application developments, we used and tested the feasibility of a wide array of laser power levels (10, 20, 30, 50 mW) and colors (green, red). In this work, we predominantly demonstrated visible green lasers for ease of development and troubleshooting. In real-world applications, invisible infrared lasers can be used to minimize intrusiveness.

Different types of cameras Additionally, we tested a wide variety of cameras including the IDS Imaging U3-3060CP, ELP 5.0 megapixel, and 2.0 megapixel USB Camera. We found the high camera frame rate to be an important factor in capturing clearer speckles that are easier to track. Low-frame-rate cameras can be used for slower applications of force. To track sudden applications of force with low-frame-rate cameras, we can also use blur detection, which is commonly adopted for laser speckle contrast imaging in clinical applications. Even though blur detection focuses more on

the presence of force, it still can enable use cases such as on-world touch segmentation.

Open source We open source our algorithms and dataset to facilitate others' use of *ForceSight*. We hope the joint force behind this technique could further advance it and enable an even more diverse set of applications with practical uses. The source code and data are available at https://github.com/forcesight/ForceSight.

8 LIMITATION

ForceSight has two main limitations which we plan to work on in future work. These limitations are around the compatibility of materials, and sensing range & resolution.

First, *ForceSight* works with many everyday surfaces with a few exceptions – plastically deformable materials, discontinuous materials, very stiff materials, and transparent materials. To begin with, *ForceSight* requires deformation delivery. Plastically deformable materials, e.g., Play-Doh, cannot transfer the deformation from the contact point to its surroundings. Second, discontinuous materials like fur and polar fleece could not work with *ForceSight*, because the force applied at one point will not be passed on to its surrounding regions. Third, *ForceSight* cannot work with stiff surfaces that are too hard to deform, e.g., a thick wood table, or concrete floor. Finally, *ForceSight* does not work with transparent surfaces. Laser beams pass through them, generating extremely dim speckles beyond the sensitivity of our system.

We also plan to optimize *ForceSight* for 1) extreme large forces (e.g., car parking on the driveway) and 2) high sensing resolution (e.g., coin on the table). Achieving these requires us to have cameras with better performance (e.g., faster speed, denser pixels on the CCD sensor) and force meters that can provide more fine-grained data in future work.

9 CONCLUSION

We present *ForceSight*, a non-contact force sensing technique using laser speckle imaging. We derived models for both the formation and motion of laser speckles induced by the deformation of rough surfaces at force. We developed and evaluated our system with a series of tests featuring different materials, sensing distances, as well as calibration methods. Results indicate the high accuracy of *ForceSight* across test settings. We conclude the paper with four applications showcasing the strength of *ForceSight* in different use cases. Overall, we believe *ForceSight* opens up new force sensing opportunities and novel interaction modalities, which could be readily integrated into many real-world applications and future computing systems.

REFERENCES

[1] David Briers, Donald D Duncan, Evan R Hirst, Sean J Kirkpatrick, Marcus Larsson, Wiendelt Steenbergen, Tomas Stromberg, and Oliver B Thompson. 2013. Laser speckle contrast imaging: theoretical and practical limitations. *Journal of biomedical optics* 18, 6 (2013), 066018.

[2] J David Briers and Sian Webster. 1996. Laser speckle contrast analysis (LASCA): a nonscanning, full-field technique for monitoring capillary blood flow. *Journal of biomedical optics* 1, 2 (1996), 174–179.

[3] Álvaro Cassinelli, Stéphane Perrin, and Masatoshi Ishikawa. 2005. Smart laser-scanner for 3D human-machine interface. In *CHI'05 Extended Abstracts on Human Factors in Computing Systems*. 1138–1139.

[4] Abe Davis, Katherine L Bouman, Justin G Chen, Michael Rubinstein, Fredo Durand, and William T Freeman. 2015. Visual vibrometry: Estimating material properties from small motion in video. In *Proceedings of the ieee conference on computer vision and pattern recognition*. 5335–5343.

[5] Home Depot. 2022. Plywood – Columbia Forest Products. https://www.homedepot.com/p/Columbia-Forest-Products-1-2-in-x-2-ft-x-2-ft-PureBond-Red-Oak-Plywood-Project-Panel-Free-Custom-Cut-Available-2847/204771237 Last accessed 24 July 2022.

[6] Mustafa Doga Dogan, Steven Vidal Acevedo Colon, Varnika Sinha, Kaan Akşit, and Stefanie Mueller. 2021. SensiCut: Material-Aware Laser Cutting Using Speckle Sensing and Deep Learning. In *The 34th Annual ACM Symposium on User Interface Software and Technology*. 24–38.

[7] Andrew K Dunn, Hayrunnisa Bolay, Michael A Moskowitz, and David A Boas. 2001. Dynamic imaging of cerebral blood flow using laser speckle. *Journal of Cerebral Blood Flow & Metabolism* 21, 3 (2001), 195–201.

[8] Berthy T Feng, Alexander C Ogren, Chiara Daraio, and Katherine L Bouman. 2022. Visual vibration tomography: Estimating interior material properties from monocular video. In *Proceedings of the IEEE/CVF Conference on Computer Vision and Pattern Recognition*. 16231–16240.

[9] Wido Heeman, Wiendelt Steenbergen, Gooitzen M van Dam, and E Christiaan Boerma. 2019. Clinical applications of laser speckle contrast imaging: a review. *Journal of biomedical optics* 24, 8 (2019), 080901.

[10] Roy Henderson and Karl Schulmeister. 2003. *Laser safety*. CRC Press.

[11] Yu-Chih Huang, Tyson L Ringold, J Stuart Nelson, and Bernard Choi. 2008. Non-invasive blood flow imaging for real-time feedback during laser therapy of port wine stain birthmarks. *Lasers in Surgery and Medicine: The Official Journal of the American Society for Laser Medicine and Surgery* 40, 3 (2008), 167–173.

[12] Vikram Iyer, Elyas Bayati, Rajalakshmi Nandakumar, Arka Majumdar, and Shyamnath Gollakota. 2018. Charging a smartphone across a room using lasers. *Proceedings of the ACM on Interactive, Mobile, Wearable and Ubiquitous Technologies* 1, 4 (2018), 1–21.

[13] Kensei Jo, Mohit Gupta, and Shree K Nayar. 2015. Spedo: 6 dof ego-motion sensor using speckle defocus imaging. In *Proceedings of the IEEE International Conference on Computer Vision*. 4319–4327.

[14] David Kim, Otmar Hilliges, Shahram Izadi, Alex D Butler, Jiawen Chen, Iason Oikonomidis, and Patrick Olivier. 2012. Digits: freehand 3D interactions anywhere using a wrist-worn gloveless sensor. In *Proceedings of the 25th annual ACM symposium on User interface software and technology*. 167–176.

[15] KyungDuk Kim, HyeonSeung Yu, Joonyoung Koh, Jung H Shin, Wonhee Lee, and YongKeun Park. 2016. Remote sensing of pressure inside deformable microchannels using light scattering in Scotch tape. *Optics Letters* 41, 8 (2016), 1837–1840.

[16] Gierad Laput and Chris Harrison. 2019. SurfaceSight: a new spin on touch, user, and object sensing for IoT experiences. In *Proceedings of the 2019 CHI Conference on Human Factors in Computing Systems*. 1–12.

[17] Dengfeng Li, Xinhong Liu, Yizhi Liang, Jun Fan, and Lidai Wang. 2019. A Low-Cost Portable Nanophotonic Sensor Based on a Smartphone: A system readily available for many applications. *IEEE Nanotechnology Magazine* 13, 3 (2019), 6–12.

[18] Camillo Lugaresi, Jiuqiang Tang, Hadon Nash, Chris McClanahan, Esha Uboweja, Michael Hays, Fan Zhang, Chuo-Ling Chang, Ming Yong, Juhyun Lee, et al. 2019. Mediapipe: A framework for perceiving and processing reality. In *Third Workshop on Computer Vision for AR/VR at IEEE Computer Vision and Pattern Recognition (CVPR)*, Vol. 2019.

[19] Thomas Henry Gordon Megson. 2019. *Structural and stress analysis*. Butterworth-Heinemann.

[20] Alex Olwal, Andrew Bardagjy, Jan Zizka, and Ramesh Raskar. 2012. SpeckleEye: gestural interaction for embedded electronics in ubiquitous computing. In *CHI'12 Extended Abstracts on Human Factors in Computing Systems*. 2237–2242.

[21] Joseph A Paradiso. 1997. The LaserWall. *The LaserWall* (1997). http://paradiso.media.mit.edu/SpectrumWeb/captions/Laser.html

[22] Joseph A Paradiso, Kai-Yuh Hsiao, Joshua Strickon, and Peter Rice. 2000. New sensor and music systems for large interactive surfaces. In *ICMC*. Citeseer.

[23] Ashwin B Parthasarathy, Erica L Weber, Lisa M Richards, Douglas J Fox, and Andrew K Dunn. 2010. Laser speckle contrast imaging of cerebral blood flow in humans during neurosurgery: a pilot clinical study. *Journal of biomedical optics* 15, 6 (2010), 066030.

[24] Santa Monica Plastics. 2022. Plastic – Santa Monica Plastics. https://santamonicaplastics.com/shop/acrylic-sheets-more-cut-to-size/cut-to-size-clear-white/acrylic-sheets-cut-to-size-opaque-white-7328/ Last accessed 24 July 2022.

[25] Munehiko Sato, Shigeo Yoshida, Alex Olwal, Boxin Shi, Atsushi Hiyama, Tomohiro Tanikawa, Michitaka Hirose, and Ramesh Raskar. 2015. Spectrans: Versatile material classification for interaction with textureless, specular and transparent surfaces. In *Proceedings of the 33rd Annual ACM Conference on Human Factors in Computing Systems*. 2191–2200.

[26] Valkyrie Savage, Colin Chang, and Björn Hartmann. 2013. Sauron: embedded single-camera sensing of printed physical user interfaces. In *Proceedings of the 26th annual ACM symposium on User interface software and technology*. 447–456.

[27] Martin Schmitz, Mohammadreza Khalilbeigi, Matthias Balwierz, Roman Lissermann, Max Mühlhäuser, and Jürgen Steimle. 2015. Capricate: A fabrication pipeline to design and 3D print capacitive touch sensors for interactive objects. In *Proceedings of the 28th Annual ACM Symposium on User Interface Software & Technology*. 253–258.

[28] Mark Sheinin, Dorian Chan, Matthew O'Toole, and Srinivasa G Narasimhan. 2022. Dual-Shutter Optical Vibration Sensing. In *Proceedings of the IEEE/CVF Conference on Computer Vision and Pattern Recognition*. 16324–16333.

[29] CJR Sheppard and M Hrynevych. 1992. Diffraction by a circular aperture: a generalization of Fresnel diffraction theory. *JOSA A* 9, 2 (1992), 274–281.

[30] Yi Chang Shih, Abe Davis, Samuel W Hasinoff, Frédo Durand, and William T Freeman. 2012. Laser speckle photography for surface tampering detection. In *2012 IEEE Conference on Computer Vision and Pattern Recognition*. IEEE, 33–40.

[31] Brandon M Smith, Pratham Desai, Vishal Agarwal, and Mohit Gupta. 2017. CoLux: Multi-object 3d micro-motion analysis using speckle imaging. *ACM Transactions on Graphics (TOG)* 36, 4 (2017), 1–12.

[32] Brandon M Smith, Matthew O'Toole, and Mohit Gupta. 2018. Tracking multiple objects outside the line of sight using speckle imaging. In *Proceedings of the IEEE Conference on Computer Vision and Pattern Recognition*. 6258–6266.

[33] Metal Supermarkets. 2022. Metal – Metal Supermarkets. https://www.metalsupermarkets.com/product/aluminum-sheet-5052/ Last accessed 24 July 2022.

[34] Nobukatsu Takai, T Iwai, and Toshimitsu Asakura. 1983. Correlation distance of dynamic speckles. *Applied Optics* 22, 1 (1983), 170–177.

[35] Yasuhiro Tamaki, Makoto Araie, Eizo Kawamoto, Shuichiro Eguchi, and Hitoshi Fujii. 1994. Noncontact, two-dimensional measurement of retinal microcirculation using laser speckle phenomenon. *Investigative ophthalmology & visual science* 35, 11 (1994), 3825–3834.

[36] Will J Warren, Erik A Moro, Matthew E Briggs, and Eric B Flynn. 2014. Simulating translation-induced laser speckle dynamics in photon Doppler velocimetry. *Applied Optics* 53, 21 (2014), 4661–4668.

[37] Karl Willis, Eric Brockmeyer, Scott Hudson, and Ivan Poupyrev. 2012. Printed optics: 3D printing of embedded optical elements for interactive devices. In *Proceedings of the 25th annual ACM symposium on User interface software and technology*. 589–598.

[38] Nan Wu and S Haruyama. 2020. Real-time audio detection and regeneration of moving sound source based on optical flow algorithm of laser speckle images. *Optics Express* 28, 4 (2020), 4475–4488.

[39] Robert Xiao, Chris Harrison, and Scott E Hudson. 2013. WorldKit: rapid and easy creation of ad-hoc interactive applications on everyday surfaces. In *Proceedings of the SIGCHI Conference on Human Factors in Computing Systems*. 879–888.

[40] Robert Xiao, Chris Harrison, Karl DD Willis, Ivan Poupyrev, and Scott E Hudson. 2013. Lumitrack: low cost, high precision, high speed tracking with projected m-sequences. In *Proceedings of the 26th annual ACM symposium on User interface software and technology*. 3–12.

[41] Robert Xiao, Scott Hudson, and Chris Harrison. 2016. Direct: Making touch tracking on ordinary surfaces practical with hybrid depth-infrared sensing. In *Proceedings of the 2016 ACM International Conference on Interactive Surfaces and Spaces*. 85–94.

[42] Robert Xiao, Scott Hudson, and Chris Harrison. 2017. Supporting responsive cohabitation between virtual interfaces and physical objects on everyday surfaces. *Proceedings of the ACM on Human-Computer Interaction* 1, EICS (2017), 1–17.

[43] Yang Zhang, Wolf Kienzle, Yanjun Ma, Shiu S Ng, Hrvoje Benko, and Chris Harrison. 2019. ActiTouch: Robust touch detection for on-skin AR/VR interfaces. In *Proceedings of the 32nd Annual ACM Symposium on User Interface Software and Technology*. 1151–1159.

[44] Yang Zhang, Gierad Laput, and Chris Harrison. 2018. Vibrosight: Long-range vibrometry for smart environment sensing. In *Proceedings of the 31st Annual ACM Symposium on User Interface Software and Technology*. 225–236.

[45] Yang Zhang, Sven Mayer, Jesse T Gonzalez, and Chris Harrison. 2021. Vibrosight++: City-Scale Sensing Using Existing Retroreflective Signs and Markers. In *Proceedings of the 2021 CHI Conference on Human Factors in Computing Systems*. 1–14.

[46] Jan Zizka, Alex Olwal, and Ramesh Raskar. 2011. SpeckleSense: fast, precise, low-cost and compact motion sensing using laser speckle. In *Proceedings of the 24th annual ACM symposium on User interface software and technology*. 489–498.